

Time-resolved x-ray scattering study on quantum materials

Xinyi Jiang(蒋心怡), Qingzheng Qiu(仇清正), and Yingying Peng(彭莹莹)
Citation: Chin. Phys. B, 2025, 34 (**10**): 107801. DOI: 10.1088/1674-1056/adfa7b
http://cpb.iphy.ac.cn; http://iopscience.iop.org/cpb

What follows is a list of articles you may be interested in

Effects of helium ion irradiation and thermal annealing on the optical and structural properties of hexagonal boron nitride

Guan-Lin Liu(刘冠麟), Ji-Lian Xu(徐辑廉), Peng-Tao Jing(景鹏涛), Jing-Jing Shao(邵京京), Xu Guo(郭旭), Yun-Tao Wu(吴韵涛), Feng Qin(覃凤), Zhen Cheng(程祯), Deming Liu(刘德明), Yang Bao(鲍洋), Hai Xu(徐海), Li-Gong Zhang(张立功), Da Zhan(詹达), Jia-Xu Yan(闫家旭), Lei Liu(刘雷), and De-Zhen Shen(申德振)
Chin. Phys. B, 2025, 34 (**5**): 057801. DOI: 10.1088/1674-1056/adbee7

Photoinduced Floquet higher-order Weyl semimetal in C_6 symmetric Dirac semimetals

Xin-Xin Xu(许欣欣), Zi-Ming Wang(王梓名), Dong-Hui Xu(许东辉), and Chui-Zhen Chen(陈垂针)
Chin. Phys. B, 2024, 33 (**6**): 067801. DOI: 10.1088/1674-1056/ad4634

Tuning energy transfer efficiency in quantum dots mixture by controling donor/acceptor ratio

Chang Liu(刘畅), Jing Liang(梁晶), Fangfang Wang(王芳芳), Chaojie Ma(马超杰), Kehai Liu(刘科海), Can Liu(刘灿), Hao Hong(洪浩), Huaibin Shen(申怀彬), Kaihui Liu(刘开辉), and Enge Wang(王恩哥)
Chin. Phys. B, 2021, 30 (**12**): 127802. DOI: 10.1088/1674-1056/ac29b2

Optical study on intermediate-valence compounds $Yb_{1-x}Lu_xAl_3$

J L Lv(吕佳林), J L Luo(雒建林), N L Wang(王楠林)
Chin. Phys. B, 2018, 27 (**1**): 017803. DOI: 10.1088/1674-1056/27/1/017803

Review of ultrafast spectroscopy studies of valley carrier dynamics in two-dimensional semiconducting transition metal dichalcogenides

Dong Sun(孙栋), Jia-Wei Lai(赖佳伟), Jun-Chao Ma(马骏超), Qin-Sheng Wang(王钦生), Jing Liu (刘晶)
Chin. Phys. B, 2017, 26 (**3**): 037801. DOI: 10.1088/1674-1056/26/3/037801

INVITED REVIEW

Time-resolved x-ray scattering study on quantum materials

Xinyi Jiang(蒋心怡), Qingzheng Qiu(仇清正), and Yingying Peng(彭莹莹)†

International Center for Quantum Materials, School of Physics, Peking University, Beijing 100871, *China*

(Received 6 June 2025; revised manuscript received 29 July 2025; accepted manuscript online 12 August 2025)

Quantum materials have attracted a great deal of attention because of their rich landscape of electronic structures, topological phases, strong correlation effects, and exotic orders. These systems provide a fertile platform for the exploration of novel quantum phenomena and materials applications. Particularly exciting is the exploration of nonequilibrium dynamics in quantum materials, which has significant research and potential application values. Pump–probe techniques play a key role in revealing the dynamics of quantum materials on remarkably short timescales, providing an attractive yet challenging avenue of research. In this context, time-resolved x-ray as an emerging probe exhibits high time resolution, momentum resolution, and substantial momentum coverage. It can reveal unprecedented transient states, distinguish between entangled ordered states, and has a compelling potential to probe ultrafast dynamics in a wide variety of quantum materials. Despite its unique advantages, time-resolved x-ray scattering still faces several technological and methodological challenges. In this review, we highlight recent advances focusing on the use of time-resolved x-ray scattering to probe dynamic processes in quantum materials. We discuss representative examples across structural, electronic, magnetic, and lattice degrees of freedom, and outline promising directions for future research in this rapidly evolving field.

Keywords: time-resolved x-ray, quantum materials, pump–probe technique, non-equilibrium dynamics

PACS: 78.47.J–, 78.47.je, 61.05.C–

DOI: 10.1088/1674-1056/adfa7b **CSTR:** 32038.14.CPB.adfa7b

1. Introduction

Quantum materials have attracted significant attention due to their unconventional electronic structures and the emergence of novel quantum phenomena.[1] These materials often exhibit pronounced quantum effects, such as tunneling, entanglement, and superconductivity. The category encompasses a wide range of material classes, including high-temperature superconductors, topological insulators, Weyl semimetals, and van der Waals materials.[2–8] Owing to their unique structural and electronic characteristics, quantum materials give rise to extraordinary phenomena across electronic, optical, and magnetic regimes, highlighting their vast potential for diverse technological applications. In particular, they serve as versatile platforms for exploring emergent quantum behavior and for investigating quantum information science. The research advances in this field are pivotal for the development of next-generation electronics, quantum computing, and energy technologies.

The strong coupling between lattice, spin, and orbital degrees of freedom in quantum materials gives rise to rich and complex phase diagrams. Under non-equilibrium conditions, these materials can exhibit a range of unprecedented transient phenomena, such as subtle electronic structure modulations, photoinduced phase transitions and elementary excitations. These transient states often elude traditional equilibrium-based measurement techniques due to their ultrafast and dynamic nature. Pump–probe spectroscopy has emerged as a powerful approach for investigating the non-equilibrium dynamics, enabling direct observation of transient changes in microscopic degrees of freedom.[9] In a typical pump–probe experiment (Fig. 1), the sample is excited by a strong laser pulse known as a pump pulse, which triggers a transient response, leading to novel phenomena such as structural deformations, electronic excitations, or phase transitions. These changes occur on an ultrafast timescale, typically spanning from femtoseconds (fs) to picoseconds (ps). Subsequently, a time-delayed probe pulse interacts with the sample, probing the time evolution of optical, electrical, or structural properties, and the scattered (or transmitted) beam is collected by the detector.

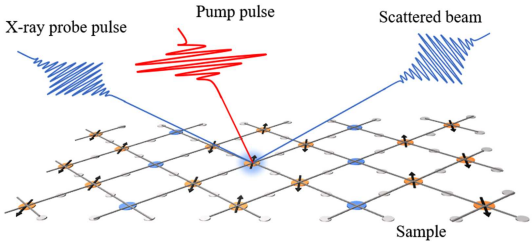


Fig. 1. A sketch of pump–probe experimental technique configuration.

Optical pulses (e.g., ultraviolet, infrared, or visible light) are commonly used as pump sources to excite the sample. Weak pump pulses can perturb the ground state, whereas

†Corresponding author. E-mail: yingying.peng@pku.edu.cn

© 2025 Chinese Physical Society and IOP Publishing Ltd. All rights, including for text and data mining, AI training, and similar technologies, are reserved.

strong pulses can drive transitions to non-equilibrium phases. Structural information is obtained through a separate probe beam (e.g., x-ray or electron) scattered by the crystal lattice. Periodically arranged atoms cause constructive interference along specific directions, forming diffraction patterns that reveal the crystal structure of the sample. The lattice dynamics triggered by coherent phonon excitation can be traced by monitoring changes in Bragg peak position and peak intensity.[11] In addition, since the symmetry of the material determines the diffraction pattern, the occurrence of phase transition will break the symmetry of the material and change the diffraction pattern, which can be tracked by the time-resolved probe pulses.[12,13] Remarkably, the charge and spin order phase in the material can also be perturbed by pump pulses, allowing the probe of transient dynamics associated with charge order and magnetic order.[14]

Table 1. Information of XFEL facilities.[10]

	European XFEL	LCLS	LCLS-II, CuRF	LCLS-II, SCRF	SACLA	SwissFEL	PAL-XFEL	SHINE
Location	Germany	USA	USA	USA	Japan	Switzerland	South Korea	China
Start of commissioning	2016	2009	2019	2020	2011	2016	2016	2025
Number of light flashes per second	27000	120	120	1000000	60	100	60	1000000
Minimum wavelength of the laser	0.05 nm	0.15 nm	0.05 nm	0.25 nm	0.08 nm	0.1 nm	0.06 nm	0.05 nm
Maximum electron energy	17.5 GeV	14.3 GeV	15 GeV	5 GeV	8.5 GeV	5.8 GeV	10 GeV	8 GeV
Peak brilliance	5×10^{33}	2×10^{33}	2×10^{33}	1×10^{33}	1×10^{33}	1×10^{33}	1.3×10^{33}	1×10^{33}
			($2{,}75\times10^{34}$ with seeding)					

In pump–probe experiments, x-rays have emerged as powerful probe pulses, enabling the investigation of ultrafast structural and electronic dynamics with atomic-scale resolution. Recent advancements in plasma technology and the development of free-electron lasers (FELs) have significantly propelled the field of time-resolved x-ray science.[15,16] In FELs, high-energy electrons are accelerated to near-light speeds using linear accelerators and directed through periodic magnetic structures (undulators), where they emit coherent electromagnetic radiation. This radiation is amplified through a self-amplified spontaneous emission process, ultimately producing highly coherent, intense, and ultrashort x-ray pulses. Technological breakthroughs have led to remarkable improvements in key parameters of x-ray FELs, including peak brightness, repetition rate, pulse duration, and coherence. Several state-of-the-art x-ray free electron laser (XFEL) facilities are currently operational or in development around the world, such as the European XFEL (Germany), LCLS-II (USA), SwissFEL (Switzerland), PAL-XFEL (Republic of Korea) and the Shanghai Coherent Light Facility (China)[17] (see more details in Table 1).[10] In particular, facilities such as the LCLS and European XFEL have demonstrated the ability to generate x-ray pulses with durations of only a few femtoseconds.[18] These pulses exhibit peak brightness up to 10^{33} photons/s/mm^2/mrad^2/0.1%BW at 1 keV, defined as the number of photons emitted per second, per square millimeter of source area, per square milliradian of solid angle, and per 0.1% bandwidth of the central photon energy, as shown in Fig. 2, far exceeding that of conventional synchrotron sources.[19–23] The exceptional characteristics of XFELs make them indispensable tools for time-resolved studies of quantum materials. They enable the direct observation of transient states and fundamental excitations, opening new avenues for research not only in condensed matter physics but also in life sciences, chemistry, and materials science.

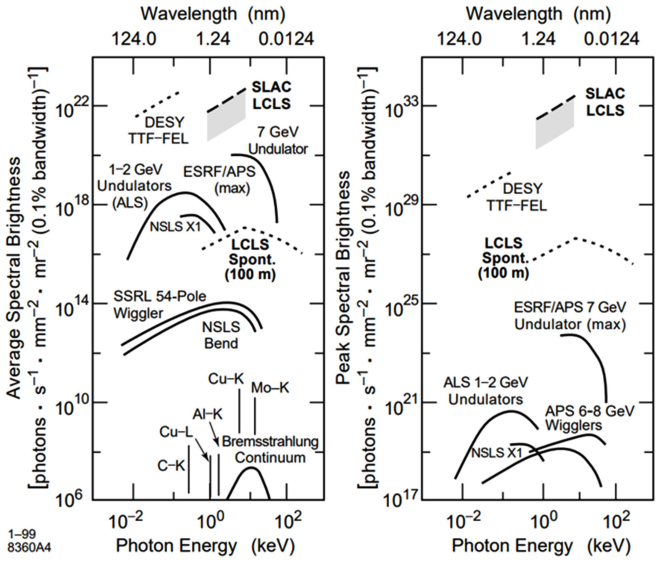


Fig. 2. Average and peak brightness (photons/s/mm^2/mrad^2/0.1%BW) calculated for the LCLS and for other facilities operating or under construction.[19]

Time-resolved x-ray scattering techniques offer several key advantages over other time-resolved probes, such as angle-resolved photoemission spectroscopy (tr-ARPES),[31,32] optical spectroscopy,[33,34] and ultrafast electron diffraction (UED).[35,36] These advantages arise from fundamental properties of x-rays: (1) Their deep penetration enables bulk-sensitive measurements, with probing depths ranging from microns (soft x-rays) to centimeters (MeV-scale hard x-rays). (2) They provide element- and orbital-specific sensitivity via resonant enhancement at absorption edges, where cross-sections can increase by factors of 10^2–10^4 through intermediate core-hole excitations.[37] (3) They afford high momentum resolution, thanks to their Ångström-scale wavelengths ($\lambda \approx$ 0.01–100 Å) and advanced focusing optics. Unlike tr-ARPES, which primarily probes surface electronic band structures, time-resolved x-ray techniques access bulk collective excita-

tions (e.g., magnons, phonons) and symmetry-broken orders (e.g., magnetic, charge, and orbital order) via momentum- and energy-resolved scattering. Additionally, because x-ray wavelengths are much closer to interatomic spacings than optical wavelengths, these techniques offer superior momentum resolution and broader momentum coverage compared to time-resolved optical probes, making them particularly powerful for studying structural dynamics. Whereas UED mainly captures lattice motions through elastic scattering, x-ray techniques probe a broader range of degrees of freedom — including electronic, magnetic, and structural — through both resonant diffraction and inelastic scattering channels. Crucially, x-rays bypass the stringent surface quality requirements imposed by tr-ARPES and UED, enabling studies of heterogeneous materials, encapsulated devices, and micron-scale single crystals with minimal sample preparation constraints. To facilitate a direct comparison, we provide a quantitative summary in Table 2, contrasting spatial, temporal, and momentum resolution, depth sensitivity, energy resolution, and sample constraints across the key time-resolved x-ray scattering techniques featured in this review (tr-XRD, tr-REXS, tr-RIXS), alongside tr-ARPES and UED.

Table 2. Comparison between XFELs, Tr-ARPES and UED techniques.

Techniques	Spatial resolution	Temporal resolution	Depth sensitivity	Momentum resolution	Energy resolution	Sample constraints
tr-XRD	tens of μm limited by x-ray spot	∼ 10 to 300 fs[24]	penetration ∼ 10–100 μm at 5–20 keV x-rays	0.001 Å^{-1}–0.01 Å^{-1}[24]	–	solids or liquids, no vacuum needed for hard x-ray
tr-REXS	tens of μm limited by x-ray spot	∼ 10 to 300 fs[25]	penetration ∼ 10–100 μm (hard x-rays); ∼ 0.1 μm (soft x-rays)	0.01 Å^{-1}	–	solids or liquids, UHV for soft x-ray edges
tr-RIXS	tens of μm limited by x-ray spot	∼ 10 to 300 fs[26]	penetration ∼ 10–100 μm (hard x-rays); ∼ 0.1 μm (soft x-rays)	0.01 Å^{-1}–0.05 Å^{-1}[26]	10 to 100 s meV level according to Heisenberg limit[26]	solids or liquids, UHV for soft x-ray edges
tr-ARPES	micro- to nano-scale (spot ≤ 10 μm; nano-ARPES ∼ 100 nm)[27]	< 10 fs[28]	surface-limited (1 ∼ 2 nm)	0.05 Å^{-1}–0.1 Å^{-1}[28]	10 to 100 s meV level according to Gaussian Fourier limit	ultrahigh vacuum and flat, conducting, clean samples
UED (MeV)	≲ 0.1 nm[29]	∼ 10 fs (state-of-art)[30]	thin-film (< 100 nm)	0.001 Å^{-1}–0.01 Å^{-1}[30]	–	radiation-tolerant, thin samples

In this review, we examine recent advances in time-resolved x-ray studies of quantum materials, with a focus on structural dynamics, phonon excitations, charge-order melting and recovery, and ultrafast magnetic phenomena. We highlight several experimental studies that have leveraged time-resolved x-ray scattering to unravel the intricate interplay between electronic, lattice, and spin degrees of freedom in strongly correlated systems, topological phases, and low-dimensional heterostructures. By synthesizing these developments, this review aims to present a comprehensive and integrated perspective on the current state of the field. In addition, we outline emerging challenges and opportunities that are likely to shape future directions in the study of ultrafast dynamics using x-ray techniques.

2. Time-resolved resonant x-ray study on quantum materials

In quantum materials, the lattice, spin, charge and orbital degrees of freedom are highly entangled, resulting in complex phase diagrams. Understanding the novel transient states is of great interest in the field of condensed matter physics.

2.1. Structure dynamics

Most two-dimensional (2D) layered materials are cleavable transition-metal chalcogenides and halides, with weak interlayer interactions. These materials include van der Waals (vdW) insulators, such as MPX_3 materials (M = transition metal, X = S or Se),[38,39] semimetals, such as $Cr_2(Si,Ge)_2Te_6$ and transition metal dichalcogenide MX_2 (M = transition metal, X = S, Se or Te).[40–44] These 2D materials with weak interlayer interactions provide a good platform for studying structural degrees of freedom, and ultrafast techniques provide interesting insights into the structure dynamics.

Faran Zhou *et al.* used time-resolved x-ray diffraction measurements to study the vdW material $FePS_3$ (Fig. 3), which were performed at the 7ID-C beamline of the Advanced Photon Source (APS) with the 400 nm pump laser pulse (fluence up to 10 mJ/cm^2) and 11 keV x-ray probe. Three Bragg peaks (002, $\bar{2}02$, $0\bar{2}2$) were measured as a function of delay time to reconstruct the dynamics of its unit cell.[45] The interlayer shear has been largely overlooked due to the weak vdW interaction. The recovery time (τ_β) of β is remarkably longer than the thermal relaxation process of the (002) peak when the temperature increased to 117 K near the magnetic transition T_N. It indicates a strong correlation between interlayer shear and magnetic order. In addition, similar structural dynamics are also observed in $NiPS_3$, which confirms universal spin-shear coupling in zigzag antiferromagnets. In contrast, $MnPS_3$, hosting Néel-type rather than zigzag order, shows no critical slowing of shear dynamics, implying that interlayer shear selectively couples with zigzag magnetic configurations. These observations demonstrate magnetoelastic coupling between structural degrees of freedom and intralayer magnetism, resulting in anisotropic structural dynamics within 2D layered materials.

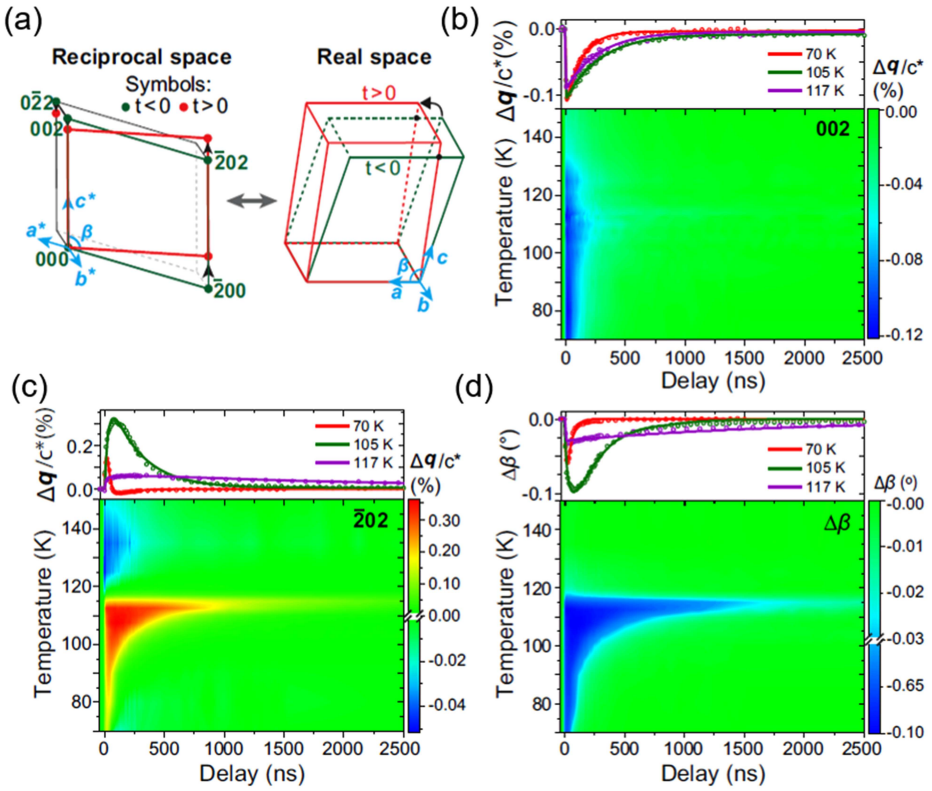


Fig. 3. Temperature-dependent structural dynamics in $FePS_3$. (a) Schematics of the reciprocal- and real-space unit cell before (green) and after (red) laser excitation. (b) Dynamics of the (002) peak shift (Δq) along the c^* direction as a function of temperature. (c) Dynamics of the ($\bar{2}02$) peak shift as a function of temperature. (d) Dynamics of β change ($\Delta\beta$) as a function of temperature.[45]

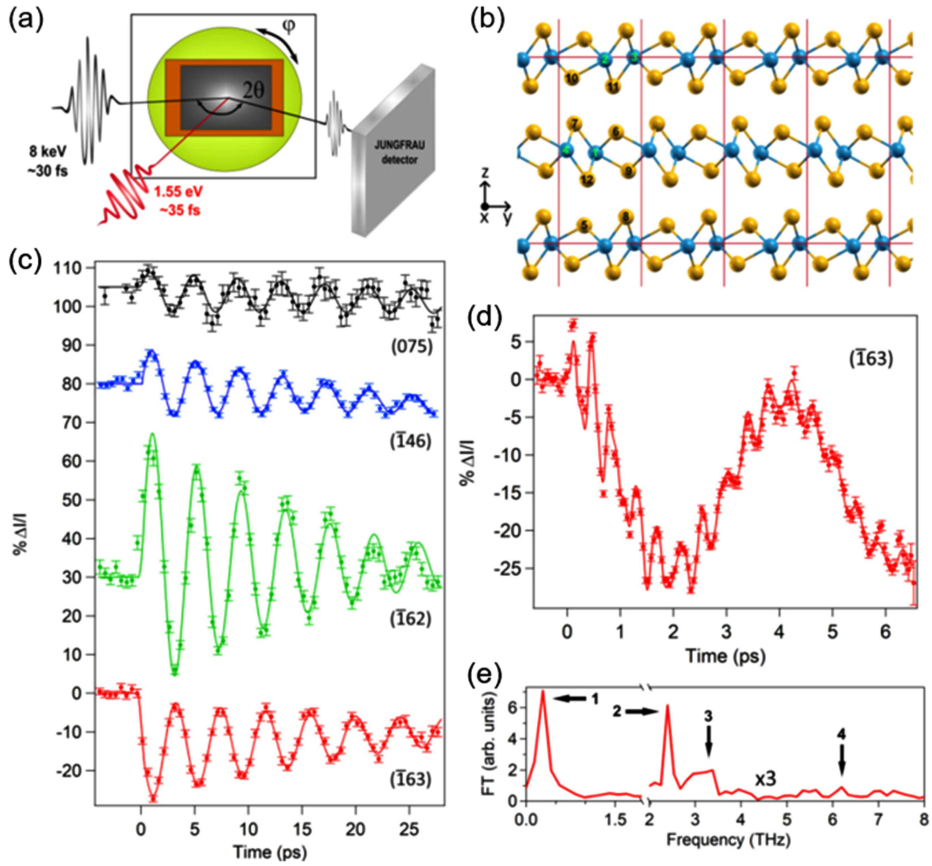


Fig. 4. Experimental scheme and time-resolved x-ray diffraction results of WTe_2. (a) Scheme of the time-resolved x-ray diffraction experiment. (b) WTe_2 crystal structure projected in the yz plane, where the red rectangles delineate the orthorhombic unit cell. (c) Time-resolved modification of the diffraction intensity $\Delta I/I$ for the (075), ($\bar{1}$46), ($\bar{1}$62), and ($\bar{1}$63) diffraction peaks. (d) Time-resolved modification of $\Delta I/I$ for the ($\bar{1}$63) reflection using a tenfold shorter time step. (e) Fourier transform of panel (d) after subtracting the non-oscillatory response. The data were acquired at 3.2 mJ/cm^2 ($T = 295$ K).[46]

The layered transition-metal dichalcogenide WTe_2 exhibits distinct transport and topological properties intrinsically linked to its crystal structure. Coherent structural dynamics induced by near-infrared (800 nm) laser excitation with fluence of 3.2 mJ/cm^2 have been quantitatively investigated by Davide Soranzio *et al*. using time-resolved x-ray diffraction at the Bernina beamline at SwissFEL with the 8 keV x-ray probe (see Fig. 4(a)). Pump-driven atomic vibrations generate oscillatory Bragg peak intensity modulations, revealing multiple coherently excited phonon modes (Fig. 4(c)).[46] Fourier analysis identifies a dominant 0.24 THz mode with $\sim$ 20 ps coherence time, while $(\bar{1}63)$ peak dynamics resolve four distinct frequencies: 0.24 THz, 2.4 THz, 3.4 THz, and 6.1 THz (Figs. 4(d) and 4(e)). Systematic fluence-dependence studies of $(\bar{1}46)$ and $(\bar{1}63)$ peaks establish quantitative excitation thresholds and amplitude scaling laws. Density functional theory (DFT) simulations reveal corresponding displacement patterns, including the 0.24 THz acoustic shear mode featuring uniform anti-phase interlayer motion. These results demonstrate how selective vibrational excitation governs the ultrafast structural evolution of WTe_2, enabling coherent control of its topological and electronic properties.

Beyond WTe_2, analogous ultrafast studies in SnSe, a prototypical V–VI semiconductor that exhibits intrinsic lattice instability, reveal complex structural dynamics. Under equilibrium conditions, SnSe undergoes reversible transitions from its low-temperature layered phase *Pnma* to higher-symmetry structures *Cmcm* at high temperatures ($\sim$ 807 K)[47] or high pressures ($\sim$ 10.5 GPa),[48] characterized by bilayer shearing that rearranges the Sn/Se atomic positions within the *ab* plane. Yijing Huang *et al*. have tracked the temporal evolution of $(21\bar{1})$, (611), (301), and $(4\bar{1}0)$ Bragg peaks,[44] using time-resolved x-ray diffraction at LCLS with near-infrared (1.55 eV) pump at a nominal absorbed fluence of 0.8 mJ/cm^2 and 9.5 keV x-ray probe. These identify that four coherent oscillation modes correspond to A_g Raman-active phonons. Pronounced phonon softening emerges with increasing fluence, by more than 20% in the A_g^1 mode at 2.2 mJ/cm^2. First-principles DFT calculations resolve the eigendisplacements of these modes, while combined experimental-theoretical analysis demonstrates that the transient state constitutes a photoinduced *Immm* structure arising from Se/Sn band excitation, distinct from thermally driven *Cmcm* phases. Collectively, these results underscore the indispensable role of time-resolved x-ray probes in resolving atomic-scale structural dynamics that remain inaccessible to conventional spectroscopic methods.

Coherent phonon excitation occurs under intense femtosecond optical pumping, generating strain waves that propagate perpendicular to the surface of the material.[50] These collective lattice vibrations manifest as characteristic oscillations on ultrafast timescales. Time-resolved x-ray techniques, offering intrinsic femtosecond temporal resolution, enable direct observation of coherent phonon generation following photoexcitation.[51–53] Ultrafast lattice excitation typically drives coherent phonons, which in turn modulate the electronic binding energies due to electron–phonon interactions.[54] A representative study by Jonathan A. Sobota *et al*. investigated coherent phonon dynamics in the topological insulator Bi_2Te_3 using tr-ARPES and time-resolved x-ray diffraction (tr-XRD).[49] Tr-ARPES measurements revealed oscillatory shifts in the surface and bulk electronic states, with the bulk states exhibiting two phonon frequencies (1.90 THz and 4.20 THz; Figs. 5(d) and 5(f)), while the surface displayed four frequencies, including two additional modes at 1.73 THz and 3.40 THz not observed in the bulk states (Figs. 5(e) and 5(g)). To investigate the lattice origin of these modes, bulk-sensitive tr-XRD measurements were performed by monitoring transient intensity changes in the (4,4,5), (5,5,6), and (3,3,4) Bragg peaks. These experiments were carried out at the LCLS at SLAC National Accelerator Laboratory with 1.5 eV pump (p-polarized with incident fluence of 8.2 mJ/cm^2) and 9.5 keV x-ray probe. Under optical excitation, all three peaks exhibit oscillatory behavior (Figs. 5(i)–5(k)). Fast Fourier transform (FFT) analysis of the diffraction signals (Figs. 5(l) and 5(n)) reveals two distinct bulk phonon modes at 1.85 THz and 3.60 THz. The spectral contributions of these modes vary with the Bragg peak, and they are attributed to A_{1g}^1 and A_{1g}^2 lattice distortions, respectively, both involving out-of-plane (*c*-axis) displacements of Bi and Te atoms. The slightly lower frequencies observed in tr-XRD compared to tr-ARPES are attributed to the higher temperature and stronger fluence conditions in the x-ray measurements. These findings help to reconcile the long-standing discrepancy between surface-sensitive and bulk-sensitive measurements of phonon modes in topological materials. By directly probing bulk lattice dynamics, time-resolved x-ray techniques offer critical benchmarks for validating and interpreting surface-sensitive results.

TaAs, a prototypical three-dimensional topological Weyl semimeta,[57,58] has generated significant research interest due to its nontrivial band topology, exotic electronic structure, and potential applications in quantum computing/spintronics. Min-Cheol Lee *et al*. have used time-resolved x-ray diffraction to detect the time evolution of truncated rod scattering (TRS) signals in a TaAs single crystal.[55] TRS is an x-ray scattering technique sensitive to surface and interfacial structures. It detects lattice modulations on length scales longer than those captured by conventional Bragg peaks. By rotating the crystal around the surface normal vector $\boldsymbol{n}$ by a small angle $\Delta\phi$, the scattering condition $\boldsymbol{k}_\mathrm{f} - \boldsymbol{k}_\mathrm{i} = \boldsymbol{G}_{hkl} + \boldsymbol{q}$ is modified, where $\boldsymbol{q} = q\hat{n}$ is a momentum component along the surface normal. This isolates the TRS signal from Bragg diffraction, enabling the study of subtle lattice displacements. Notably, since coherent phonon scattering occurs in the same direction, tracking TRS intensity in time allows for real-time visualization

of coherent phonon dynamics. The experiment, conducted at the LCLS, used 800 nm (1.55 eV) optical pump pulses with an incident fluence of 2.86 mJ/cm^2 and a 9.52 keV x-ray probe. By adjusting the sample orientation (Figs. 6(a)–6(c)), TRS signals at different momentum transfers were selectively measured. Pronounced phonon oscillations are observed in the ultrafast dynamics. The Fourier transform of the coherent phonon oscillation clearly shows two different frequencies (Figs. 6(j)–6(l)), corresponding to the asymmetrical-shaped quasilongitudinal (QL) and symmetrical-shaped quasishear (QS) acoustic phonon modes, respectively. These chirp-model-reproducible modes exhibit momentum-dependent dispersions, with both frequencies increasing as the momentum transfer increases. Specifically, time-resolved x-ray directly maps how these phonons instantaneously modify the electronic structure near Weyl points: QL vibrations occur primarily normal to the (112) plane, while QS displacements align parallel to this plane. The simultaneous resolution of multiple phonon modes demonstrates the unique capacity of time-resolved x-ray to detect electron-phonon coupling dynamics in topological semimetals.

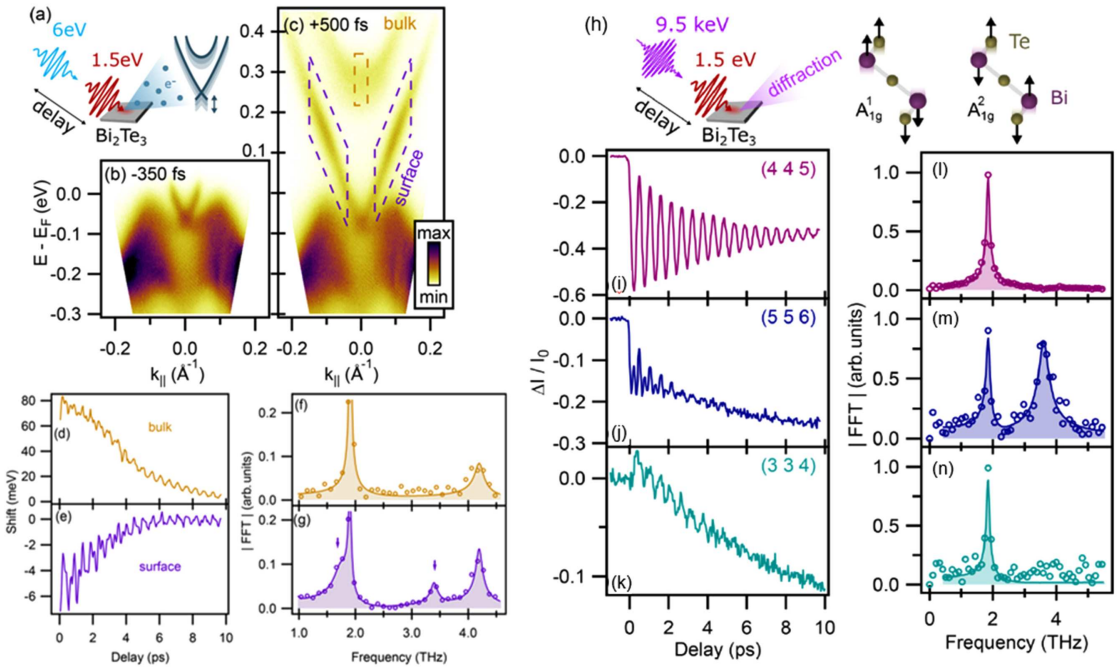


Fig. 5. Coherent phonon dynamics in Bi_2Te_3 using time-resolved ARPES and x-ray diffraction measurements. (a) Schematic of tr-ARPES measurements to measure electronic binding energy oscillations. (b) ARPES spectrum along the $\overline{\Gamma K}$ direction before and (c) after excitation at the pump–probe delays indicated. (d) Time-dependent shift in the binding energy of the bulk conduction band and (e) surface state within the energy-momentum windows indicated by dashed lines in (c). (f) Magnitude of the Fourier transform of the bulk conduction band and (g) surface state dynamics. The arrows highlight two modes observed in the surface state but not in the bulk. (h) Schematic configuration of time-resolved x-ray diffraction experiments. (i)–(k) Time-dependent relative change in the intensities of the (h, k, l) = (4, 4, 5), (5, 5, 6), and (3, 3, 4) Bragg peaks. (l)–(n) The corresponding Fourier transforms after exponential background subtraction. Points are from the data, and lines are fits.[49]

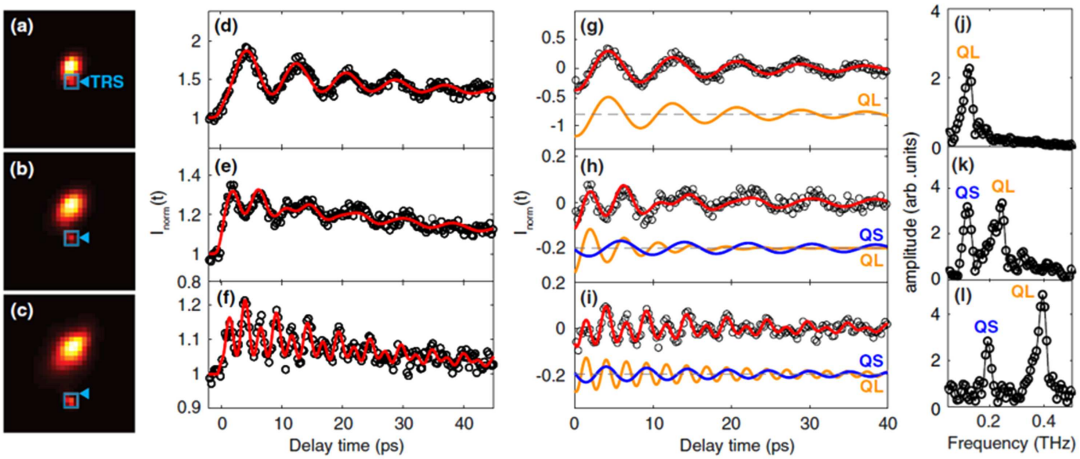


Fig. 6. The dynamics of coherent acoustic phonons in the Weyl semimetal TaAs. (a)–(c) 2D XRD images, showing diffuse scattering (non-Bragg component of the scattering signal, arising from short-range order, disorder, defects, or thermal fluctuations in the crystal) and TRS signals in the equilibrium state. Panels (a)–(c) correspond to rotation angles $\Delta\phi$ of $-0.15°$, $-0.3°$, $-0.5°$. As the rotation angle $\Delta\phi$ increases, so does the momentum. (d)–(f) Time-resolved TRS signal traces, integrated over the blue arrow area of the detector. (g)–(i) Experimental data of extracted oscillations. (j)–(l) The fast Fourier transform of the coherent phonon oscillations.[55]

2.2. Charge order dynamics

High-temperature superconductivity is one of the most remarkable discoveries, yet its underlying mechanism remains elusive. Superconductivity (SC) often emerges in proximity to symmetry-breaking states such as antiferromagnetic order or charge order (CO).[59,60] In recent years, CO, frequently manifested as a charge density wave (CDW), has been found to be ubiquitous across a wide range of superconducting cuprates.[61–65] However, its relationship with SC remains a topic of intense debate. A growing body of research suggests that CO competes with or becomes intertwined with SC.[66,67] Resonant elastic x-ray scattering (REXS), also known as resonant soft x-ray scattering (RSXS), involves tuning the incident x-ray energy to an element-specific absorption edge to enhance sensitivity to specific electronic states. It does not distinguish the energy of the scattering photons and is particularly effective for probing static order parameters, such as charge, orbital, and magnetic orders, with elemental and orbital specificity. Moreover, resonance conditions amplify the scattering cross section, greatly enhancing sensitivity to weak magnetic and charge orders. Consequently, time-resolved REXS has emerged as a powerful technique for investigating the dynamics of CO and spin order on ultrafast timescales. This method is indispensable for disentangling their intertwined behaviors and for uncovering the fundamental interactions that govern high-temperature superconductivity.

Scott Wandel *et al.* have used ultrafast resonant soft x-ray scattering to track the CDW dynamics of underdoped $YBa_2Cu_3O_{6.67}$ ($T_c = 65$ K) in superconducting and normal states.[56] Time-resolved pump–probe experiments were performed at LCLS with the 800 nm pump and 931.5 eV x-ray probe. In the normal states ($T \sim T_c$), the pump-induced CDW intensity is rapidly suppressed and the correlation length is almost unchanged, with the recovery time of around 3 ps (Fig. 7(b)). However, in the superconducting state, suppression of SC is observed by ultrafast optical measurements, while enhancement of CDW is detected by time-resolved x-ray scattering (Fig. 7(c)). This indicates the competitive relationship between CO and SC. Most interestingly, in the superconducting state ($T = 12$ K), the CDW correlation length doubles relative to equilibrium (Fig. 7(d), right panel), indicating the formation of a topological defect analogous to tritelluride systems.[35,69] These findings suggest that SC disrupts the spatial coherence of the CDW within CDW domains by stabilizing topological defects, such as discommensurations.

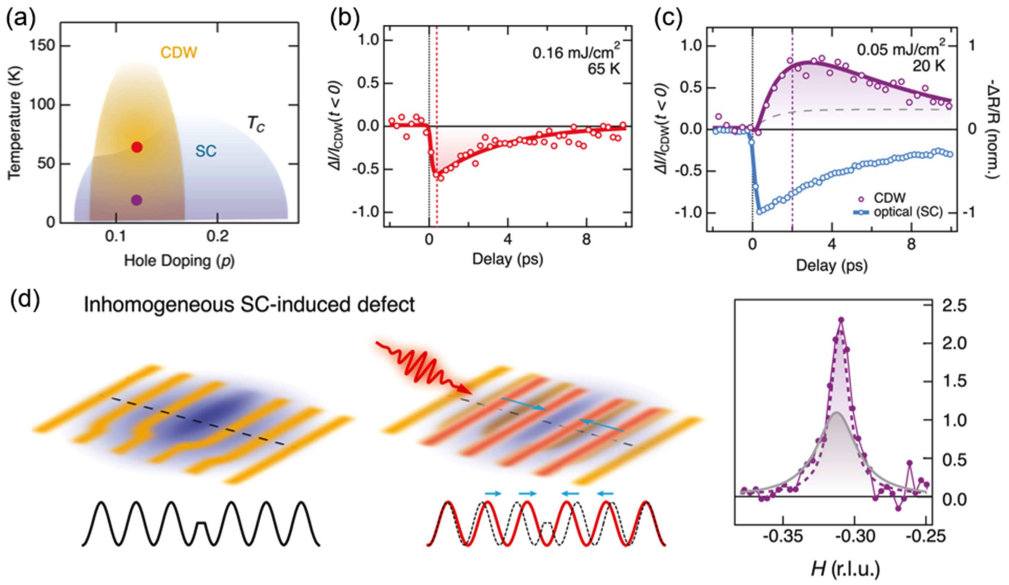


Fig. 7. CDW and SC dynamics in $YBa_2Cu_3O_{6.67}$ and scenarios for their interactions. (a) Schematic phase diagram of $YBa_2Cu_3O_{6.67}$ showing the two temperatures, within (20 K) and just above (65 K) the SC dome for $x = 0.67$ (hole doping $p = 0.12$). (b) CDW signal at 65 K as a function of the delay time, with laser pump fluence of 0.16 mJ/cm^2. (c) Optical (blue circles) and x-ray scattering (purple circles) signals measuring the SC and CDW dynamics, respectively, at 20 K with laser fluence of 0.05 mJ/cm^2. (d) The most probable model of the spatial arrangements of CDW and SC regions before and after photoexcitations.[56]

Photoinduced enhancement of CDW in the superconducting state and suppression of CDW in the normal state have also been observed by Hoyoung Jang *et al.* using ultrafast resonant soft x-ray scattering performed at PAL-XFEL with the 800 nm pump pulse at fluence of 15 μJ/cm^2 and 931.5 eV x-ray probe.[68] In Fig. 8(a), a slight reduction in CDW intensity at 65 K ($\sim T_c = 65.5$ K) can be attributed to the melting of CDW by the pump laser. In the equilibrium state, the CDW intensity reaches its maximum near half integer ($L \sim 1.5$ r.l.u.), and the CDW becomes weak as it moves toward integer L, as shown in Fig. 8(b), which follows the typical quasi-2D CDW behavior in cuprates. Remarkably, the 800 nm laser triggers a photo-induced charge order that reaches its maximum at $L \sim 1.2$ r.l.u., close to the integer value, which resem-

bles the observation of the high magnetic field measurements (see Fig. 8(c)). This indicates that laser pulses break Cooper pairing in superconducting states, thereby leading to the nucleation of the 3D CDW precursor correlation.

The CDW dynamics in $La_{2-x}Ba_xCuO_4$ ($x = 1/8$) has been investigated by Matteo Mitrano *et al.* using time-resolved resonant soft x-ray scattering performed at LCLS.[70] Upon excitation with 800 nm laser pulses, the CDW peak intensity is rapidly suppressed within 1 ps and remains significantly diminished even after 40 ps (Fig. 9(a)). Figure 9(b) illustrates the relaxational dynamics of the charge order peak intensity in $La_{2-x}Ba_xCuO_4$ for various momenta q relative to the charge order wavevector Q_{CDW}. Each time trace is well-described by a single exponential decay and a constant offset. The extracted relaxation time shows a pronounced momentum dependence, consistent with the standard framework for relaxational dynamics of a nonconserved order parameter in a periodic system. In this description, the time evolution follows $\exp[-\gamma(q)t]$, where the relaxation rate is given by $\gamma(q) = \gamma_0 + Dq^2$, with γ_0 representing uniform dissipation and D the diffusion constant. As shown in Fig. 9(c), the relaxation rate $\hbar\gamma(q)$ increases quadratically with momentum and is well captured by this diffusive model, yielding dissipation parameter $\hbar\gamma_0 = 0.1730 \pm 0.0015$ meV and diffusion constant $\hbar D = 215 \pm 19$ meV·Å^2. These results indicate that the transverse collective excitations of the charge order propagate via Brownian diffusion. The characteristic fluctuation energy, $\hbar\gamma_0 \sim 0.17$ meV (corresponding to ~ 2 K), closely matches the superconducting transition temperature T_c near $x \sim 1/8$, suggesting a possible connection between the low-energy CDW dynamics and superconductivity in this cuprate system.

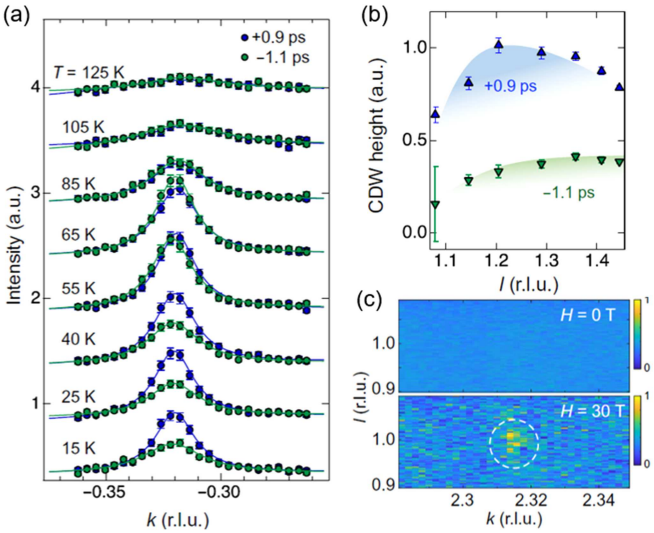


Fig. 8. Temperature and l dependence of photoinduced CDW in $YBa_2Cu_3O_{6+x}$. (a) CDW peak profiles at (0, k, ∼ 1.45) measured at $\Delta t = 0.9$ ps (blue) and 1.1 ps (green) with varying temperatures. Solid lines are Lorentzian fits to the data with a linear background. (b) Fitted CDW heights with the different l position at $\Delta t = 0.9$ ps and 1.1 ps. (c) Observed 3D CDW of YBCO via a pulsed magnet experiment. The field-induced CDW appears around (0, $2 + q_{CDW}$, 1), compared to the zero field.[68]

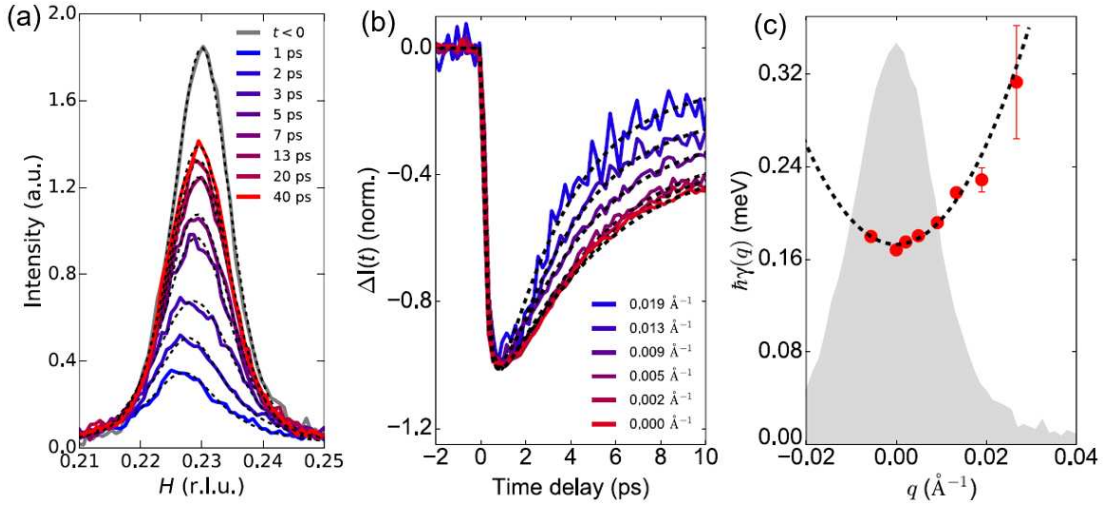


Fig. 9. Time-resolved x-ray measurements of charge order in $La_{1.875}Ba_{0.125}CuO_4$. (a) Transient charge order peak profile after excitation for a selection of time delays. (b) Time traces of the energy-integrated charge order scattering for a selection of momenta. (c) Collective modes of charge order in LBCO propagate diffusively.[70]

Charge order becomes particularly intriguing in the overdoped regime, where it demonstrates unexpected robustness, even persisting at room temperature.[64,72] Although the ultrafast dynamics of CO has been extensively explored in underdoped cuprates, much less is known about its behavior in the overdoped regime. To address this, Xinyi Jiang *et al.* recently employ time-resolved resonant x-ray scattering (tr-REXS) and x-ray absorption spectroscopy (tr-XAS) performed at PALXFEL with the 800 nm and 400 nm pump and x-ray probe to track the transient electronic density of states and CO dynamics in overdoped $(Bi,Pb)_{2.12}Sr_{1.88}CuO_6$.[71] Their results reveal a striking wavelength dependence in the photoexcited response of CO in the overdoped cuprate: a 400 nm pump pulse effectively melts the CO, while an 800 nm pulse does not, indicating an orbital-selective photodoping effect (Fig. 10). To accurately track the evolution of the CO peak intensity, the resonant diffraction signal is normalized by the simultaneously recorded x-ray fluorescence yield. This normal-

ization compensates for pump-induced shifts in the x-ray absorption spectra, which affect the measured peak intensity.[71] Taking into account this absorption change, the authors isolate the intrinsic dynamics of charge order. The recovery time of the CO ($\sim$ 3 ps) closely matches that observed in underdoped systems, suggesting a universal electronic instability across doping levels. However, in contrast to the underdoped regime, melting CO in the overdoped state requires nearly an order of magnitude higher pump fluence, highlighting the stabilizing role of lattice interactions at high doping levels. These findings shed new light on the microscopic origin of CO in overdoped cuprates and demonstrate the potential of ultrafast optical control to manipulate ordering phases in correlated materials.

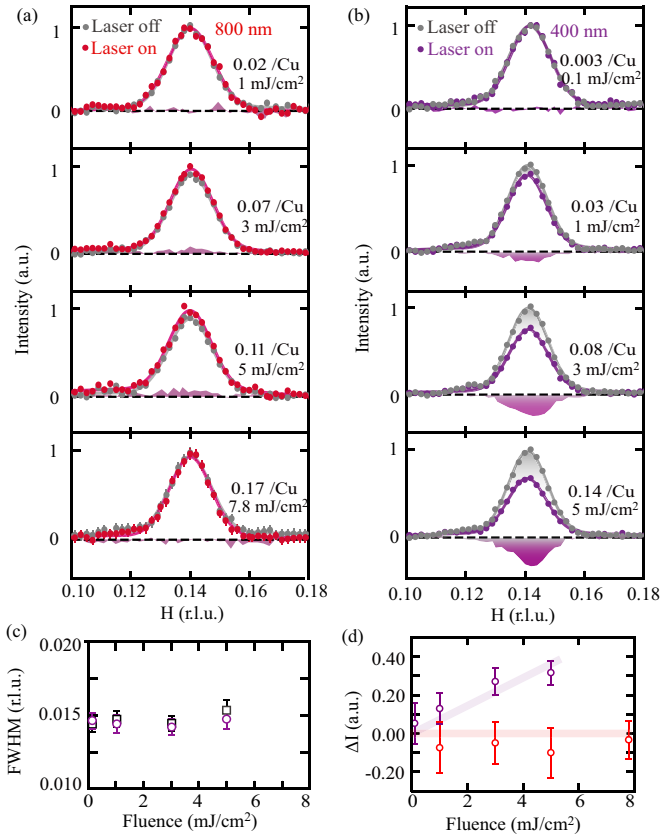


Fig. 10. Pump-induced change in CO peak for 800 nm and 400 nm pumps. The evolution of the CO scattering peak divided by the fluorescent signal with different laser fluences for 800 nm (a) and 400 nm (b) pumps at $\Delta t = 0.25$ ps at 80 K. The purple shading indicates the difference between photo-induced states and equilibrium states. Solid lines are Lorentzian fits to the data with a linear background. (c) Fitted peak width (FWHM) of CO peaks before (black square) and after (purple circle) 400 nm excitation as a function of fluence. The error bars represent 1 standard deviation (s.d.) of the fit parameters. (d) Changes in CO intensity induced by 800 nm (red marker) and 400nm (purple marker) pumps.[71]

Kagome superconductors, with their unique lattice structure and non-trivial band topology, exhibit exotic electronic phases. The recent discovery of kagome metals, particularly CsV_3Sb_5, has sparked intense research interest due to the CDW, SC, intertwined symmetry breaking, and topological properties. Among these, CDWs play a pivotal role in mediating the interplay between various competing orders, including orbital flux states, electronic nematicity, and SC.[74–76] Apart from 1×4 modulation observed by several STM experiments,[77] CsV_3Sb_5 also exhibits $2 \times 2 \times 1$, $2 \times 2 \times 2$ and $2 \times 2 \times 4$ CDWs stacking phases, where the $2 \times 2 \times 2$ CDW reconstructions prevail in CsV_3Sb_5 and compete with the $2 \times 2 \times 4$ stacking.[78] There are two types of $2 \times 2 \times 2$ CDWs-MLL phase with alternative aligned star-of-David (SD) and inverse star-of-David (ISD) stacking, and LLL phase with staggered ISD stacking. Understanding the nature and dynamics of these CDW phases is crucial for unraveling the complex phase diagram and unconventional SC observed in kagome systems. Recently, Honglie Ning *et al.* have tracked the dynamics of CDW peaks after light excitation using time-resolved x-ray diffraction performed at LCLS with the near infrared (0.6 eV) laser pulse and 9.835 keV x-ray probe.[73] The opposite behaviors in peak widths in the MLL and LLL phases, triggered by photoexcitation, have revealed the coexistence and competition between the two different CDW phases in CsV_3Sb_5, as shown in Fig. 11. By probing the real-time evolution of the CDW orders, time-resolved x-ray scattering deciphers the intricate phase relationships and sheds light on the complex interplay between competing phases underlying kagome superconductivity.

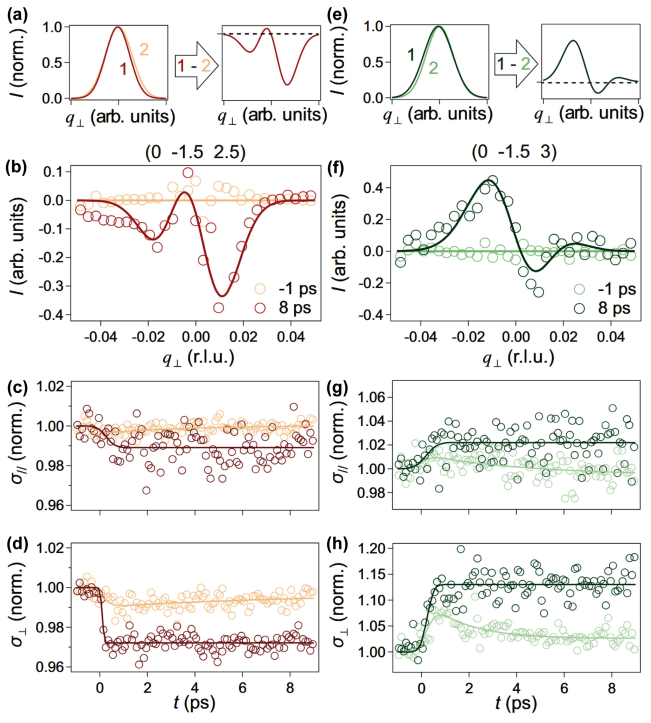


Fig. 11. Dynamics of the CDW peak width revealing the competition between CDWs. (a) Schematics of the differential peak-intensity-normalized line cuts along $q_\perp$. Peak 1 indicates the CDW peak after laser excitation ($t = 8$ ps), and peak 2 indicates the CDW peak before excitation ($t = -1$ ps). (b) Differential peak-intensity-normalized line cuts along $q_\perp$ acquired at $t = 1$ ps and $t = 8$ ps of the peak at (0, -1.5, 2.5). Solid lines are fits to zero constant and subtraction of two Gaussians, respectively. (c), (d) Temporal evolution of the (0, -1.5, 2.5) peak width along $q_\parallel$ and $q_\perp$ directions pumped at $F = 0.25$ (light orange) and 2.5 mJ/cm^2 (dark red) normalized by their equilibrium values. Solid lines are fits to a single exponential decay. (e) Schematics of the differential peak-intensity-normalized line cuts along $q_\perp$. (f)–(h) Same plots as panels (b)–(d) but for the peak at (0, -1.5, 3).[73]

Chirality, characterized by the absence of mirror symmetry and the presence of handedness, is a fundamental property that influences phenomena across a wide range of scientific disciplines. Chiral phases represent a frontier of research, as they can host unconventional transport, topological properties, and symmetry-breaking mechanisms not accessible in achiral systems. Recent studies employing Raman spectroscopy, inelastic x-ray scattering, and resonant x-ray scattering have revealed the chiral electronic order in the transition metal dichalcogenide 1T-$TiSe_2$ in equilibrium states.[80,81] Understanding the nature and dynamics of electronic chirality is critical for elucidating how symmetry breaking leads to the emergence of novel functionalities and could pave the way for the development of new paradigms for light-controlled quantum states. Recently, Qingzheng Qiu *et al*. employ tr-XRD with circularly polarized pump lasers to investigate the photoinduced dynamics of chirality in 1T-$TiSe_2$.[79] For the first time, a pronounced circular dichroism in the intensity of a CDW peak under circularly polarized light excitation was observed, as shown in Fig. 12(a). Furthermore, the authors observed a transient decrease in half-width at half-maximum (HWHM) of Lorentz components in Voigt profile fitting, which is usually related to crystallite size.[82] This indicates an enhancement of the CDW correlation length following circularly polarized excitation (Fig. 12(b)), suggesting a light-driven expansion of the chiral domains. These findings provide crucial insights into the mechanism driving the manipulation of chirality in 1T-$TiSe_2$, and demonstrate that tr-XRD with circularly polarized pump lasers is an effective tool for probing chirality in condensed matter systems.

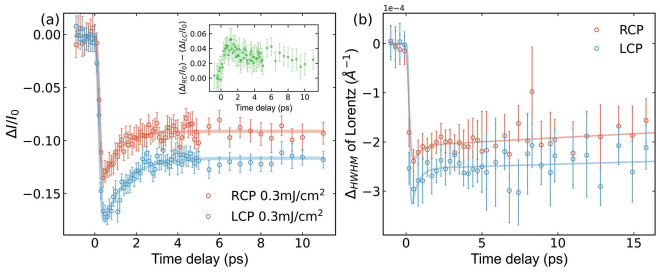


Fig. 12. Time-resolved x-ray diffraction measurements of charge density wave in $TiSe_2$.[79] (a) Time evolution of $(\frac{1}{2}, \frac{1}{2}, \frac{1}{2})$ CDW peak intensity after excited by 800 nm right circularly polarized (RCP) laser and left circularly polarized (LCP) laser at $T = 120$ K. Colored lines illustrate the fit to a single exponential function. The green dots in the inset represent the value of variation differences between RCP and LCP pumps at different delays. (b) Time dependence of HWHM variations for Lorentz components, obtained by subtracting the fit parameters before- and after-pump, as extracted from Voigt profile fittings.[79]

2.3. Magnetic dynamics

In condensed matter physics, understanding entangled spin excitations in spin–orbit entangled systems is a longstanding pursuit. Kitaev candidate materials, a type of spin–orbit entangled insulator, have recently stimulated significant research due to their exotic quantum magnetism. Among this class, $Na_2Co_2TeO_6$ exhibits complicated spin interactions and a diverse magnetic phase diagram. However, the diffuse low-energy spin excitations below the transition temperatures of 2D magnetic order (31 K) have impeded the precise determination of its spin gap. Time-resolved experiments can be used to study excitations in the μeV energy range by converting from the time domain to energy domain, making them complementary to inelastic x-ray and neutron scattering.[85,86] Using $Na_2Co_2TeO_6$ as an example, Xinyi Jiang *et al*. study these low-energy spin excitations using the time-resolved resonant elastic x-ray scattering (tr-REXS) performed at PAL-XFEL with the 400 nm laser pulse.[83] Their observations reveal remarkably slow spin dynamics at the magnetic peak, with a recovery timescale of several nanoseconds (Fig. 13). This recovery timescale aligns with the extrapolated spin gap of ~ 1 μeV obtained by density matrix renormalization group (DMRG) simulations in the thermodynamic limit. The consistency demonstrates the efficacy of tr-REXS in discerning low-energy spin gaps inaccessible to conventional spectroscopic techniques. This novel methodology can achieve unprecedented accuracy and has the potential to explore systems with gap sizes ranging from sub-μeV to meV. This approach opens new avenues for understanding and characterizing spin phenomena.

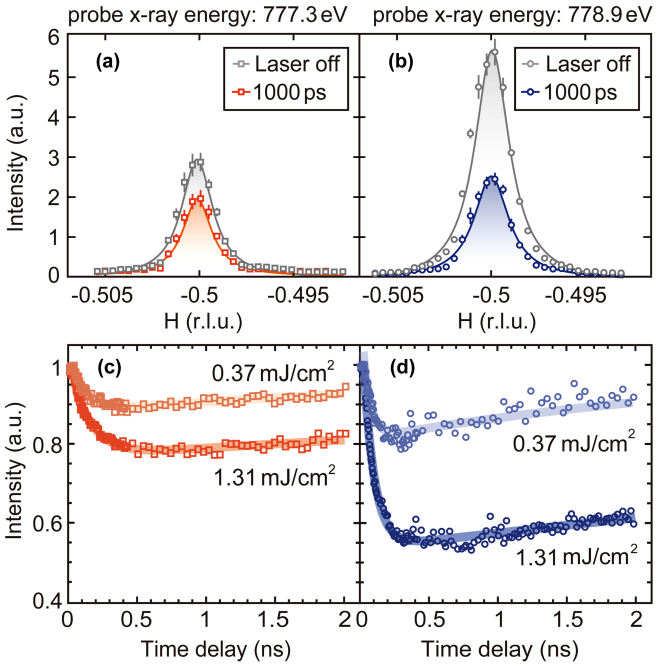


Fig. 13. Destruction and recovery of magnetic diffraction with a 400 nm excitation. (a), (b) The variation of the (−0.5, 0, 0.62) magnetic peak before and after pump excitation (1000 ps, 400 nm) with 777.3 eV and 778.9 eV at 23 K. The superstructure peaks are subtracted from the data. The grey shade indicates the change in intensity caused by photoexcitation. Solid lines are fit using a Lorentzian function. Error bars represent Poisson counting error. (c), (d) Magnetic intensity normalized by laser-off data as a function of time delay with 777.3 eV (c) and 778.9 eV (d) at 23 K. The blue and red lines display the results of fitting, corresponding to pump fluence of 0.37 mJ/cm^2 and 1.31 mJ/cm^2, respectively.[83]

In addition to using magnetic dynamics to measure the spin gap, manipulation of magnetism using ultrafast laser

pulses has also been the focus of intense research, as magnetic excitations are central to many phenomena, including unconventional SC, CDW, and quantum spin liquids.[14,59,87,88] The use of time-resolved x-ray scattering is a crucial approach for examining the intricate dynamics associated with magnetic order and magnetic excitations. Its application is pivotal in understanding the emergence and characteristics of novel quantum states.[89,90]

Coherent quasiparticle excitations associated with the magnetic order, unlike well-defined coherent phonons, are rarely observed in equilibrium measurements because of feeble signals and lack of clear identification. $Ba_{0.5}Sr_{1.5}Zn_2(Fe_{1-x}Al_x)_{12}O_{22}$ (BSZFAO), a rare room-temperature magnetoelectric material, exhibits magnetically-induced ferroelectricity with transverse conical ferromagnetic (FM) and antiferromagnetic (AFM) orders, as shown in Fig. 14(a).[91] In BSZFAO ($x = 0.08$), Hoyoung Jang *et al.* use time-resolved resonant x-ray scattering at PAL-XFEL to reveal strong oscillations at AFM (0, 0, $3n \pm 1.5$) and FM (0, 0, $3n$) peaks with excitation of 400 nm laser (Fig. 14(b)).[84] These oscillations vanish at off-resonant energy, confirming their origin as coherent 41.7 GHz (~ 0.17 meV) magnons rather than coherent phonons. Further validation comes from applied magnetic field studies (200 mT), where similar oscillations persist (Figs. 14(c) and 14(d)). Displacive coherent magnon excitation generates substantial long-lived photoinduced magnetic fields (~ 200 mT).[92] The photoinduced magnetic field is as strong as that of most rare-earth permanent magnets. Not only 400 nm laser, 800 nm lasers can also generate a photo-induced magnetic field, but the efficiency is lower than that of 400 nm, requiring 25 times higher fluence to achieve up to 200 mT magnetic fields. The observed difference in photoinduced magnetic responses originates from fundamentally distinct microscopic excitation pathways at different pump wavelengths. Under 400 nm excitation, the displacive excitation of coherent magnons mechanism is activated via charge transfer between multivalent Fe ions. This process, occurring above the bandgap, leads to a long-lived photoinduced magnetic anisotropy (PMA) that effectively acts as a transient internal magnetic field, coherently driving magnon oscillations. In contrast, 800 nm excitation primarily induces intra-ionic d–d transitions, which do not facilitate valence exchange and thus generate only a weak PMA, resulting in a significantly reduced magnon response. This wavelength-dependent behavior provides critical mechanistic insight into how optical pumping selectively drives coherent spin dynamics in multiferroic systems. Time-resolved x-ray scattering directly visualizes pump-triggered coherent magnons, establishing its indispensability for probing ultrafast photo-magnetic coupling.

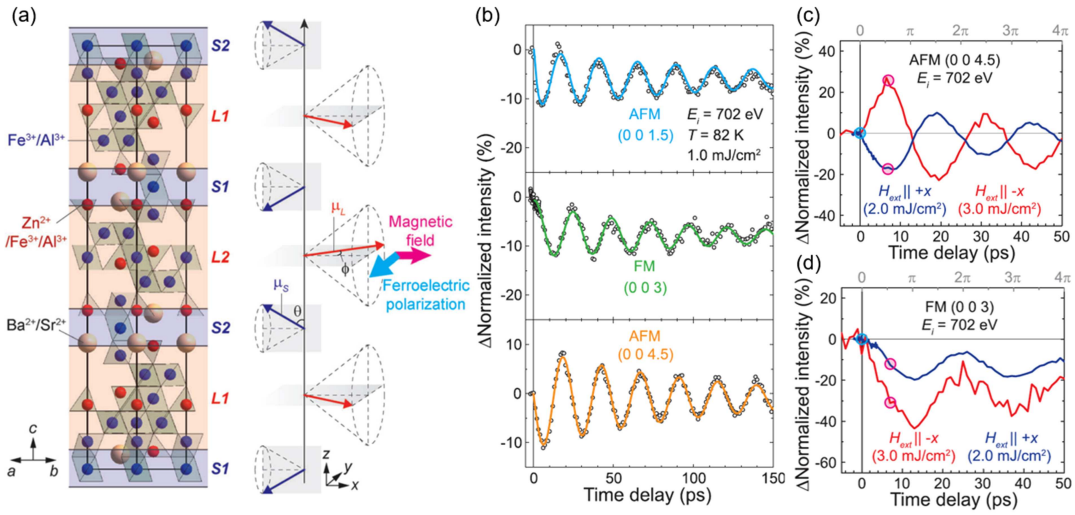


Fig. 14. Transient magnetic Bragg peak intensities with excitation of 400 nm laser in BSZFAO. (a) Crystal and magnetic structures of the Y-type hexaferrite. (b) AFM (0, 0, 1.5) (top), FM (0, 0, 3) (middle), and AFM (0, 0, 4.5) (bottom) reflections at $T = 82$ K for a laser fluence of 1.0 mJ/cm^2 using $E_i = 702$ eV. The solid lines are fitting results combining a damped oscillation and an exponential decay. (c), (d) AFM (0, 0, 4.5) and FM (0, 0, 3) reflections for $H_{ext} \parallel x$ (2.0 mJ/cm^2) and x (3.0 mJ/cm^2) at $T = 82$ K.[84]

Topological insulators, characterized by insulating bulk states and gapless metallic surface states, represent a distinct class of quantum materials that are defined by symmetry-protected topological invariants, which fundamentally distinguish them from trivial insulators. $MnBi_2Te_4$ is an intrinsic magnetic topological material in which the magnetic order arises from localized Mn 3d spins and is intricately coupled to the topological band structure composed of the itinerant Bi and Te p states.[94] This unique coexistence of magnetism and topology has made $MnBi_2Te_4$ a model system for investigating the interplay between localized and itinerant spins using ultrafast techniques. Hari Padmanabhan *et al.* have revealed contrasting transient magnetic responses of these spin subsystems. The ultrafast demagnetization of itinerant p states, with a decay time of 5 ps, has been observed via time-resolved electron diffuse scattering combined with magneto-optic Kerr ef-

fect (MOKE) measurements.[94] In contrast, the dynamics of localized Mn 3d spins have been probed using time-resolved resonant soft x-ray scattering carried out at beamline 4-ID-C at APS with the 1030 nm (1.2 eV) pump pulses, revealing two distinct demagnetization channels. A slow decay process, extending over hundreds of picoseconds, is attributed to spin–lattice coupling, reflecting the inertial nature of localized moments. In addition, a faster demagnetization component, occurring within tens of picoseconds (below the experimental resolution of 90 ps), provides clear evidence of strong exchange coupling between Mn 3d spins and the itinerant p electrons. This coupling, quantified through Landau–Lifshitz–Gilbert (LLG) simulations, yields an estimated exchange interaction strength of $J_{\rm pd} \simeq 20$ meV. This represents the first experimental determination of the exchange interaction between localized and itinerant spins in an intrinsic magnetic topological material using time-resolved x-ray techniques. More broadly, these findings establish time-resolved x-ray scattering as a powerful method for probing the coupling between magnetism and topological electronic states, offering a pathway to uncover the dynamic behavior of correlated spin and charge in complex quantum materials.

In addition to resonant elastic x-ray scattering, resonant inelastic x-ray scattering (RIXS) provides a powerful extension by analyzing the energy loss of scattered photons, granting direct access to a broad spectrum of elementary excitations, including magnons, orbital excitations, and phonons, with energy resolutions down to tens of meV. RIXS is uniquely suited for probing low-energy dynamics and collective excitations, offering both momentum- and energy-resolved information. Time-resolved RIXS (tr-RIXS) combines these spectral capabilities with femtosecond temporal resolution, enabling the direct mapping of nonequilibrium energy–momentum landscapes in quantum materials. Unlike tr-REXS, which is primarily sensitive to changes in order parameters (e.g., magnetic, charge, structural, or orbital order), tr-RIXS can resolve dynamical evolution of elementary excitations, such as magnon decay, phonon thermalization, and orbital spectral transfer, throughout the Brillouin zone. This unique capability makes tr-RIXS an indispensable tool for quantifying transient many-body effects and ultrafast processes, such as photoinduced phase transitions and correlated-electron thermalization. For instance, in correlated insulators like $Sr_3Ir_2O_7$ and Sr_2IrO_4,[95,96] tr-RIXS directly visualizes the ultrafast evolution of magnetic dynamics, capturing the transient softening and recovery of spin waves (from ∼100 meV to ∼150 meV) and the behavior of orbital excitations (∼ 680 meV) at both the magnetic Brillouin zone center (π, π) and boundary (π, 0). These measurements reveal how spin gaps, magnon dispersion, and interlayer coupling shape the recovery pathways on femtosecond-to-nanosecond timescales.

Intriguingly, recent theoretical advances have demonstrated the potential of tr-RIXS to probe spin fluctuations in nonequilibrium quantum materials. Using a nonequilibrium extension of the two-dimensional single-band Hubbard model, a recent study calculated the time-resolved magnetic excitation spectrum in a Mott insulator on a square lattice.[93] The simulations reveal a pump-induced softening of the spin excitations, attributed to both photodoping effects and Floquet renormalization of the exchange interaction. These changes are captured in the calculated magnon dispersion (Fig. 15(b)) and detailed tr-RIXS spectra across different doping levels (Figs. 15(c)–15(h)). Notably, this approach quantitatively describes the short-range paramagnon dynamics in hole-doped Mott insulators. For example, the Floquet linear spin-wave theory (FLSW) successfully reproduces the magnitude of paramagnon softening observed at 16.7% doping. These results underscore the power of nonequilibrium many-body theory in revealing the microscopic mechanisms underlying ultrafast magnetic dynamics.

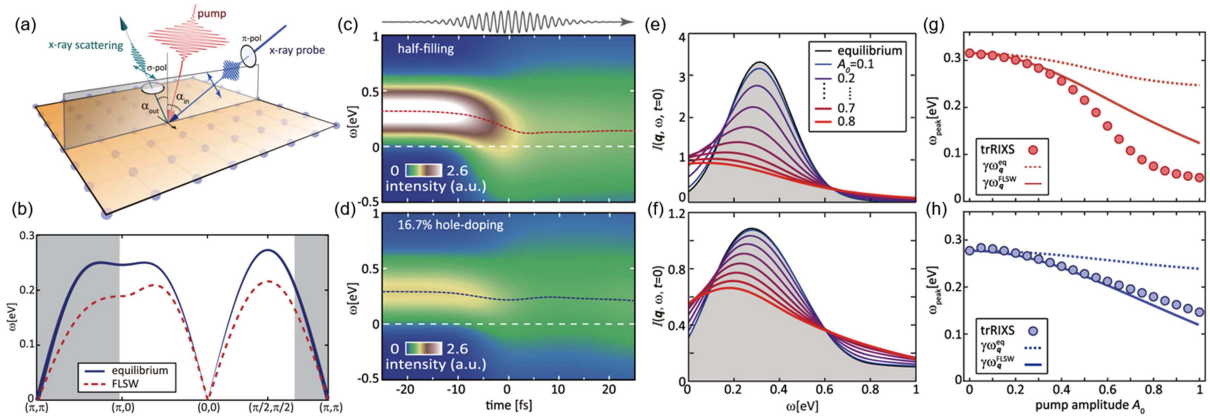


Fig. 15. Photoinduced dynamics of finite-momentum spin excitations in two-dimensional Mott insulators. (a) Sketch of the tr-RIXS experiment with π–σ polarization. (b) Magnon dispersion in the 2D Hubbard model in (blue solid line) and out of equilibrium (red dashed line, pump field amplitude $A_0 = 0.6$). (c), (d) Time evolution of the cross-polarized tr-RIXS spectra for pump energy $\Omega = 10t_{\rm h}$ and amplitude $A_0 = 0.6$ at (c) $x = 0$ and (d) $x = 0.167$ doping. (e), (f) tr-RIXS spectra at $t = 0$ (center of the pump pulse) for variable pump amplitudes. (g), (h) Spin excitation energy ω_q (the peak of the tr-RIXS intensity) as function of the pump amplitude.[93]

3. Conclusion and outlook

The rapid advancement of time-resolved x-ray methodologies has established them as a versatile experimental platform for investigating nonequilibrium dynamics. Characterized by exceptional temporal resolution (fs to ps) and momentum-space coverage and resolution ($\delta q/q \sim 10^{-4}$), these techniques enable the direct quantification of structural evolution in van der Waals heterostructures by ultrafast diffraction. In topological semimetals and Weyl fermion systems, they resolve nonequilibrium phonon dispersion renormalization. In addition, time-resolved resonant x-ray scattering reveals competitive dynamics between CDW and SC in underdoped cuprates, pump wavelength dependent CO dynamics in overdoped cuprates, competitive dynamics between the two coexisting CDW phases in CsV_3Sb_5, and non-equilibrium chiral CO dynamics in 1T-$TiSe_2$. For magnetic systems, element-specific x-ray diffraction probes coherent magnon excitations in ordered phases and can use the magnetic dynamics to measure small spin gaps in quantum magnets.

Despite the transformative potential of time-resolved x-ray scattering, these techniques face several experimental challenges. Prolonged exposure to high flux induces cumulative radiation damage through atomic displacement and ionization,[97] altering sample stoichiometry and crystallinity within picoseconds -manifested as the broadening of the diffraction peak or the decrease in intensity.[98] Concurrently, pump-laser fluence exceeding material-specific thresholds triggers nonthermal melting,[99] with damage thresholds depending on photon energy (e.g., infrared radiation (IR) > ultraviolet radiation (UV)). To mitigate such damage, several strategies can be employed. Cooling the sample to cryogenic temperatures using gas/liquid nitrogen or helium can significantly slow down damage accumulation. Additionally, damage can be minimized by ensuring that the x-ray pulse duration is shorter than the timescale of atomic rearrangement. Translating the position of the sample frequently to expose fresh regions is a common practice to avoid repeated exposure. For particularly damage-sensitive samples, single-shot experiments, in which the complete data set is acquired from a single FEL pulse, eliminate the need for repeated measurements and thus prevent cumulative damage altogether. The laser fluence, optical penetration depth, and signal-to-noise ratio (SNR), which are interdependent parameters, should also be carefully balanced. The penetration depth is determined by the absorption coefficient of the sample at the pump laser wavelength. Higher fluence enhances the excitation efficiency and improves SNR, but at the cost of increased heat deposition and a higher risk of sample damage. For materials with high damage thresholds, increasing the fluence is an effective strategy to enhance signal quality. In contrast, for more fragile samples, raising the repetition rate of the laser (when supported by the FEL) provides an alternative path to improve SNR without increasing per-pulse energy. The time-energy uncertainty principle ($\Delta E \cdot \Delta t \geq \hbar/2$) further imposes stringent limitations: while achieving < 100 fs temporal resolution, resonant techniques typically attain only $\Delta E \approx 100$–300 meV, insufficient for resolving features with small characteristic energy. Calibrating and synchronizing femtosecond pump–probe setups also pose significant challenges. Unlike conventional all-optical pump–probe experiments where both pump and probe pulses originate from the same laser source, time-resolved x-ray diffraction involves synchronization between two distinct light sources: a laser (pump) and an x-ray probe (from free-electron lasers or synchrotron radiation). In standard ultra-fast optical setups, temporal jitter affects both beams equally, allowing synchronization automatically. However, in time-resolved x-ray scattering experiments, the pump and probe sources are intrinsically independent, making their inherent timing jitter non-correlated and impossible to passively cancel. Consequently, precise monitoring and active correction of the pump–probe arrival time are critical to achieving femtosecond-scale temporal resolution. As shown in Refs. [100,101], specially designed electron bundle arrival time monitoring and optical non-collinear cross-correlator are used to monitor the arrival time of x-rays and lasers, respectively. With these techniques, timing jitter can be measured and corrected with better than 10 fs precision, allowing the overall experimental time resolution to approach the pulse duration limit of the FEL and laser systems.

On the theoretical side, modeling nonequilibrium dynamics remains a significant challenge. Current approaches, including the density matrix renormalization group (DMRG), Floquet theory, and time-dependent density functional theory (TDDFT), face inherent limitations: DMRG's computational cost scales exponentially with entanglement entropy,[102–105] restricting real-time simulations beyond picoseconds despite its efficacy for 1D ground states; Floquet formalism effectively describes periodically-driven systems (e.g., light-induced band topology) but fails for non-periodic drives and strongly correlated regimes;[106–108] while TDDFT solves time-dependent Kohn–Sham equations for excitonic dynamics, standard exchange–correlation functionals break down for Mott transitions and non-adiabatic processes.[109,110] Developing multiscale *ab initio* frameworks that integrate DMFT with tensor network methods remains essential for capturing strong-correlation dynamics. A comprehensive theoretical overview is beyond the scope of this manuscript, and we refer interested readers to recent reviews that survey the application of DMRG, TDDFT, DMFT, and related methods to time-resolved FEL studies.[85,111] Continued progress in these theoretical approaches is indispensable for interpreting the complex ultrafast phenomena unveiled by modern spectroscopic

techniques.

Looking ahead, we anticipate that integrating time-resolved x-ray probes with other advanced techniques will open new frontiers. For example, combining femtosecond x-ray spectroscopy with nanoscale imaging or microscopy will allow "movies" of nonequilibrium phenomena in real space. Pump–probe x-ray ptychography or scanning coherent diffraction could map transient domain dynamics or strain fields in driven materials. Similarly, coupling x-ray spectroscopies with ultrafast photoemission or electron microscopy could correlate electronic and lattice dynamics at the nanoscale.

In conclusion, time-resolved x-ray scattering is at a transformative threshold with the potential to revolutionize our understanding of driven quantum matter. As XFEL sources become brighter and more flexible and as detectors and optics improve, the attainable energy and time resolution will significantly advance. Together with more powerful theory, these advances will enable a truly comprehensive picture of driven quantum matter: tracking how electronic orders form, melt, and interplay with lattice and spin on fundamental timescales. By uniting structural and spectroscopic views of ultrafast dynamics, the field is poised to unravel the complex nonequilibrium physics and guide the design of light-controlled states.

Acknowledgements

Y.Y.P. is grateful for financial support from the National Key R&D Program of China (Grants Nos. 2024YFA1408702 and 2021YFA1401903), Beijing Natural Science Foundation (Grant No. JQ24001), and the National Natural Science Foundation of China (Grant No. 12374143).

References

[1] Keimer B and Moore J 2017 *Nat. Phys.* **13** 1045
[2] Zhou X, Lee W, Imada M, *et al*. 2021 *Nat. Rev. Phys.* **3** 462
[3] Qi X L, Zhang S C, *et al*. 2011 *Rev. Mod. Phys.* **83** 1057
[4] Sie E, Nyby C, Pemmaraju C, *et al*. 2019 *Nature* **565** 61
[5] Armitage N P, Mele E J, Vishwanath A, *et al*. 2018 *Rev. Mod. Phys.* **90** 015001
[6] Burch K, Mandrus D, Park J, *et al*. 2018 *Nature* **563** 47
[7] Wu J, Liu F, Sasase M, *et al*. 2019 *Sci. Adv.* **5** eaax9989
[8] Ahn C, Cavalleri A, Georges A, *et al*. 2021 *Nat. Mater.* **20** 1462
[9] Buzzi M, Först M, Mankowsky R, *et al*. 2018 *Nat. Rev. Mater.* **3** 299
[10] European XFEL 2023 *Facility comparison* 2023-10-01
[11] Lindenberg A M, Kang I, Johnson S L, *et al*. 2000 *Phys. Rev. Lett.* **84** 111
[12] Tsuyama T, Chakraverty S, Macke S, *et al*. 2016 *Phys. Rev. Lett.* **116** 256402
[13] Zong A, Dolgirev P E, Kogar A, *et al*. 2019 *Phys. Rev. Lett.* **123** 097601
[14] Chuang Y D, Lee W S, Kung Y F, *et al*. 2013 *Phys. Rev. Lett.* **110** 127404
[15] Murnane M M, Kapteyn H C, Rosen M D, *et al*. 1991 *Science* **251** 531
[16] Bostedt C, Boutet S, Fritz D M, *et al*. 2016 *Rev. Mod. Phys.* **88** 015007
[17] Dunne M 2018 *Nat. Rev. Mater.* **3** 290
[18] Cartlidge E 2016 *Science* **354** 22
[19] Cornacchia M 1998 *Linac coherent light source (LCLS) design study report* (No. SLAC-R-521), SLAC National Accelerator Lab, Menlo Park, CA (United States)
[20] Bao C, Tang P, Sun D, *et al*. 1998 *Nature Structural & Molecular Biology* **5** 657
[21] Altarelli M 2011 *Nucl. Instrum. Meth. Phys. Res. Sect. B* **269** 2845
[22] Tschentscher T, Bressler C, Grünert J, *et al.* 2017 *Applied Sciences* **7** 592
[23] Oloff L P, Oura M, Chainani A, *et al.* 2016 *Hard X-ray Photoelectron Spectroscopy (HAXPES)* ed Woicik J (Cham: Springer) pp. 555–568
[24] Ingold G, Abela R, Arrell C, *et al.* 2019 *Journal of Synchrotron Radiation* **26** 874
[25] Jang H, Kim H D, Kim M, Park S H, Kwon S, Lee J Y, Park S Y, Park G, Kim S, Hyun H, *et al.* 2020 *Rev. Sci. Instrum.* **91** 083904
[26] Schlappa J, Ghiringhelli G, Van Kuiken B E, *et al.* 2025 *Journal of Synchrotron Radiation* **32** 29
[27] Zhang H, Pincelli T, Jozwiak C, Kondo T, Ernstorfer R, Sato T and Zhou S 2022 *Nature Reviews Methods Primers* **2** 54
[28] Boschini F, Zonno M and Damascelli A 2024 *Rev. Mod. Phys.* **96** 015003
[29] Wang X and Li Y 2018 *Chin. Phys. B* **27** 076102
[30] Filippetto D, Musumeci P, Li R, Siwick B J, Otto M, Centurion M and Nunes J 2022 *Rev. Mod. Phys.* **94** 045004
[31] Bao C, Tang P, Sun D, *et al*. 2022 *Nat. Rev. Phys.* **4** 33
[32] Sobota J A, He Y, Shen Z X, *et al*. 2021 *Rev. Mod. Phys.* **93** 025006
[33] Pokharel A, Grigorev V, Mejas A, *et al*. 2022 *Commun. Phys.* **5** 141
[34] Claudio Giannetti Massimo Capone D F, *et al*. 2016 *Adv. Phys.* **65** 58
[35] Kogar A, Zong A, Dolgirev P E, *et al*. 2020 *Nat. Phys.* **16** 159
[36] Filippetto D, Musumeci P, Li R K, *et al*. 2022 *Rev. Mod. Phys.* **94** 045004
[37] Ament L J, Van Veenendaal M, Devereaux T P, *et al*. 2011 *Rev. Mod. Phys.* **83** 705
[38] Joy P and Vasudevan S 1992 *Phys. Rev. B* **46** 5425
[39] Burch K S, Mandrus D, Park J G, *et al*. 2018 *Nature* **563** 47
[40] Li Y, Chen Z, Wang J, *et al*. 2023 *npj 2D Mater. Appl.* **7** 39
[41] Gong C, Li L, Li Z, *et al*. 2017 *Nature* **546** 265
[42] OâHara D J, Zhu T, Trout A H, *et al*. 2018 *Nano Lett.* **18** 3125
[43] Fei Z, Zhao W, Palomaki T, *et al*. 2018 *Nature* **560** 336
[44] Huang Y, Yang S, Teitelbaum S, *et al*. 2022 *Phys. Rev. X* **12** 011029
[45] Zhou F, Hwangbo K, Zhang Q, *et al*. 2022 *Nat. Commun.* **13** 6598
[46] Soranzio D, Savoini M, Beaud P, *et al*. 2022 *npj 2D Mater. Appl.* **6** 71
[47] Li C W, Hong J, May A F, *et al*. 2015 *Nat. Phys.* **11** 1063
[48] Loa I, Husband R, Downie R, *et al*. 2015 *J. Phys. Condens. Matter* **27** 072202
[49] Sobota J A, Teitelbaum S W, Huang Y, *et al*. 2023 *Phys. Rev. B* **107** 014305
[50] Thomsen C, Grahn H T, Maris H J, *et al*. 1986 *Phys. Rev. B* **34** 4129
[51] Sokolowski-Tinten K, Blome C, Blums J, *et al*. 2003 *Nature* **422** 287
[52] Moore R G, Lee W S, Kirchman P S, *et al*. 2016 *Phys. Rev. B* **93** 024304
[53] Trigo M, Giraldo-Gallo P, Kozina M E, *et al*. 2019 *Phys. Rev. B* **99** 104111
[54] Zeiger H, Vidal J, Cheng T, *et al*. 1992 *Phys. Rev. B* **45** 768
[55] Lee M C, Sirica N, Teitelbaum S, *et al*. 2022 *Phys. Rev. Lett.* **128** 155301
[56] Wandel S, Boschini F, da Silva Neto E, *et al*. 2022 *Science* **376** 860
[57] Zhou Y, Lu P, Du Y, *et al*. 2016 *Phys. Rev. Lett.* **117** 146402
[58] Yang L, Liu Z, Sun Y, *et al*. 2015 *Nat. Phys.* **11** 728
[59] Mathur N, Grosche F, Julian S, *et al*. 1998 *Nature* **394** 39
[60] Demler E, Sachdev S, Zhang Y, *et al*. 2001 *Phys. Rev. Lett.* **87** 067202
[61] Ghiringhelli G, Le Tacon M, Minola M, *et al*. 2012 *Science* **337** 821
[62] Wen J, Huang H, Lee S, *et al*. 2019 *Nat. Commun.* **10** 3269
[63] Peng Y, Fumagalli R, Ding Y, *et al*. 2018 *Nat. Mater.* **17** 697
[64] Li Q, Huang H Y, Ren T, *et al*. 2023 *Phys. Rev. Lett.* **131** 116002
[65] Huang H Y, Singh A, Mou C Y, *et al*. 2021 *Phys. Rev. X* **11** 041038
[66] Chang J, Blackburn E, Holmes A, *et al*. 2012 *Nat. Phys.* **8** 871
[67] Li X, Zou C, Ding Y, *et al*. 2021 *Phys. Rev. X* **11** 011007
[68] Jang H, Song S, Kihara T, *et al*. 2022 *Sci. Adv.* **8** eabk0832
[69] Orenstein G, Duncan R A, de la Pena Munoz G A, *et al.* 2023 arXiv preprint arXiv:2304.00168
[70] Mitrano M, Lee S, Husain A A, *et al*. 2019 *Sci. Adv.* **5** eaax3346
[71] Jiang X, Li Q, Qiu Q, *et al.* 2025 arXiv preprint arXiv:2506.04697
[72] Peng Y, Fumagalli R, Ding Y, *et al*. 2018 *Nat. Mater.* **17** 697
[73] Ning H, Oh K H, Su Y, *et al*. 2024 *Nat. Commun.* **15** 7286
[74] Mielke III C, Das D, Yin J X, *et al*. 2022 *Nature* **602** 245
[75] Nie L, Sun K, Ma W, *et al*. 2022 *Nature* **604** 59
[76] Lou R, Fedorov A, Yin Q, *et al*. 2022 *Phys. Rev. Lett.* **128** 036402

[77] Zhao H, Li H, Ortiz B R, *et al*. 2021 *Nature* **599** 216
[78] Xiao Q, Lin Y, Li Q, *et al*. 2023 *Phys. Rev. Res.* **5** L012032
[79] Qiu Q Z, Chun S H, Park J, *et al*. 2025 *Phys. Rev. Lett.* **135** 116904
[80] Xiao Q, Janson O, Francoual S, *et al*. 2024 *Phys. Rev. Lett.* **133** 126402
[81] Kim K, Kim H W J, Ha S, *et al*. 2024 *Nat. Phys.* **20** 1919
[82] De Keijser T H, Langford J I, Mittemeijer E J, *et al*. 1982 *J. Appl. Crystallogr.* **15** 308
[83] Jiang X, Qiu Q, Peng C, *et al*. 2025 *npj Quantum Mater.* **10** 15
[84] Jang H, Ueda H, Kim H D, *et al*. 2023 *Adv. Mater.* **35** 2303032
[85] Wang Y, Claassen M, Pemmaraju C D, *et al*. 2018 *Nat. Rev. Mater.* **3** 312
[86] Seaberg M, Holladay B, Lee J, *et al*. 2017 *Phys. Rev. Lett.* **119** 067403
[87] Balents L 2010 *Nature* **464** 199
[88] Broholm C, Cava R J, Kivelson S, *et al*. 2020 *Science* **367** eaay0668
[89] Kirilyuk A, Kimel A V, Rasing T, *et al*. 2010 *Rev. Mod. Phys.* **82** 2731
[90] Reis D A and Lindenberg A M 2006 *Light Scattering in Solid IX* (Springer) pp. 371–422
[91] Kimura T, Lawes G, Ramirez A P, *et al*. 2005 *Phys. Rev. Lett.* **94** 137201
[92] Hansteen F, Kimel A, Kirilyuk A, *et al*. 2005 *Phys. Rev. Lett.* **95** 047402
[93] Wang Y, Chen Y, Devereaux T, *et al*. 2021 *Commun. Phys.* **4** 212
[94] Padmanabhan H, Stoica V A, Kim P K, *et al*. 2022 *Adv. Mater.* **34** 2202841
[95] Dean M P, Cao Y, Liu X, *et al*. 2016 *Nat. Mater.* **15** 601
[96] Mazzone D G, Meyers D, Cao Y, *et al*. 2021 *Proc. Natl. Acad. Sci. USA* **118** e2103696118
[97] Kubin M, Kern J, Guo M, *et al*. 2018 *Phys. Chem. Chem. Phys.* **20** 16817
[98] Davis K M, Kosheleva I, Henning R W, *et al*. 2013 *J. Phys. Chem. B* **117** 9161
[99] Carr C, Radousky H, Demos S, *et al*. 2003 *Phys. Rev. Lett.* **91** 127402
[100] Angelovski A, Kuntzsch M, Czwalinna M K, *et al*. 2015 *Phys. Rev. ST Accel. Beams* **18** 012801
[101] Divall M C, Mutter P, Divall E J, *et al*. 2015 *Opt. Express* **23** 29929
[102] White S R 1992 *Phys. Rev. Lett.* **69** 2863
[103] Yan S, Huse D A, White S R, *et al*. 2011 *Science* **332** 1173
[104] Peng C, Jiang Y F, Devereaux T P, *et al*. 2021 *npj Quantum Mater.* **6** 64
[105] Depenbrock S, McCulloch I P, Schollwöck U, *et al*. 2012 *Phys. Rev. Lett.* **109** 067201
[106] Mitrano M and Wang Y 2020 *Commun. Phys.* **3** 184
[107] Chen Y, Wang Y, Claassen M, *et al*. 2020 *npj Quantum Mater.* **5** 84
[108] Rudner M and Lindner N 2020 *Nat. Rev. Phys.* **2** 229
[109] Pertot Y, Schmidt C, Matthews M, *et al*. 2017 *Science* **355** 264
[110] Garratt D, Misiekis L, Wood D, *et al*. 2022 *Nat. Commun.* **13** 3414
[111] Mitrano M and Wang Y 2020 *Commun. Phys.* **3** 184